Journal of Computational Physics 229 (2010) 7834–7847

Contents lists available at ScienceDirect

Journal of Computational Physics

journal homepage: www.elsevier.com/locate/jcp

Molecular simulations of electroosmotic flows in rough nanochannels

Jin Liu [a,*], Moran Wang [a,b], Shiyi Chen [a,c], Mark O. Robbins [a,d]

[a] Department of Mechanical Engineering, Johns Hopkins University, Baltimore, MD 21218, USA
[b] Earth and Environmental Sciences Division, Los Alamos National Laboratory, Los Alamos, NM 87545, USA
[c] State Key Laboratory for Turbulence and Complex Systems and Institute for Applied Physics and Technology, College of Engineering, Peking University, Beijing, China
[d] Department of Physics and Astronomy, Johns Hopkins University, Baltimore, MD 21218, USA

ARTICLE INFO

Article history:
Received 24 March 2010
Received in revised form 18 June 2010
Accepted 26 June 2010
Available online 30 June 2010

Keywords:
Electrokinetic transport
PPPM method
Multi-grid method
Molecular dynamics
Electroosmotic flows

ABSTRACT

A highly efficient molecular dynamics algorithm for micro and nanoscale electrokinetic flows is developed. The long-range Coulomb interactions are calculated using the Particle–Particle Particle–Mesh (P^3M) approach. The Poisson equation for the electrostatic potential is solved in physical space using an iterative multi-grid technique. After validation, the method is used to study electroosmotic flow in nanochannels with regular or random roughness on the walls. The results show that roughness reduces the electroosmotic flow rate dramatically even though the roughness is very small compared to the channel width. The effect is much larger than for pressure driven flows because the driving force is localized near the walls where the charge distribution is high. Non-Newtonian behavior is also observed at much lower flow rates. Systematic investigation of the effect of surface charge density and random roughness will help to better understand the mechanism of electrokinetic transport in rough nanochannels and to design and optimize nanofluidic devices.

1. Introduction

Electrokinetic transport at micro/nano scales is of growing theoretical interest and practical relevance in a wide range of applications. For example, electroosmotic transport plays an essential role in many biochemical and biophysical processes [1,2]. Studies of dynamics in electrolyte solutions have been performed using continuum based methods that capture average behavior and are valid at large scales [3–11]. As system dimensions decrease into the nanoscale, the discrete nature of electrical charge and the atomic structure of fluids and surfaces becomes important. This has led to increasing interest in molecular dynamics simulations [12–17]. However, the long-range nature of the Coulomb potential between charged particles presents a significant challenge to molecular simulations. Unlike Lennard–Jones and other short-ranged potentials, the Coulomb interaction can not be truncated, and direct summation is computationally prohibitive for the required system sizes. As a result, tremendous effort has been devoted to developing new algorithms that efficiently treat long-range interactions [18].

The most widely used method is Ewald summation, which was first introduced by Ewald in 1921 [19]. The total electrostatic potential is rewritten as a summation of three terms: a short-range term that is calculated in real space, a long-range term that can be evaluated analytically in reciprocal space, and a constant self-interaction term. Even with an optimized selection of parameters, the computation time still scales as $N_p^{3/2}$ [20], where N_p is the total number of particles. This makes

* Corresponding author. Present address: Department of Bioengineering, University of Pennsylvania, 240 Skirkanich Hall, Philadelphia, PA 19104, USA.
E-mail addresses: jinliu2@seas.upenn.edu (J. Liu), mwang@lanl.gov (M. Wang), syc@jhu.edu (S. Chen), mr@jhu.edu (M.O. Robbins).

0021-9991/$ - see front matter © 2010 Elsevier Inc. All rights reserved.
doi:10.1016/j.jcp.2010.06.042

the Ewald method unsuitable for simulation of large systems. Darden et al. [21] presented the Particle Mesh Ewald (PME) method in which the long-range interactions were calculated using the Fast Fourier Transform (FFT) technique on a mesh. The computation time then scales as $N_G \log(N_G)$ where N_G is the number of mesh grid points. The Fast Multipole Method (FMM) proposed by Greengard and Rokhlin [22] can scale linearly with N_p, however the implementation of the method must be carefully designed to reach the optimized scaling [23].

Beckers et al. [24] proposed a new implementation of the Particle–Particle Particle–Mesh (P^3M) method of Hockney and Eastwood [25]. Unlike previous Fourier transform based P^3M methods [25,26], they solved the Poisson equation for the electrical potential in real space using the iterative Successive Over Relaxation (SOR) technique. Compared with $N_G \log(N_G)$ scaling for the Fourier based method, this iterative scheme scales only as N_G. As pointed out in Ref. [24], solving the Poisson equation in real space had the advantages of ease of parallel implementation and flexibility for handling different types of boundary conditions. The limitation of their scheme lies in the second charge assignment step. This dominates the computation time as the mesh spacing decreases or the cutoff radius increases. They alleviate this problem by solving a diffusion equation.

In this paper we develop a highly efficient P^3M algorithm based on Beckers et al.'s work [24] and apply it to simulations of electrokinetic flows. The algorithm uses an iterative multi-grid method to solve the Poisson equation. This multi-grid method has complexity of order N_G and exhibits a much better convergence rate compared with the traditional SOR method. We overcome the second charge assignment problem using the separability property of Gaussians.

The outline of the paper is as follows. In Section 2, we describe the numerical algorithm. This includes a description of the P^3M approach, the multi-grid Poisson solver and the treatment of boundary conditions for slablike geometries. In Section 3 we first verify the code and boundary treatments by computing the electrostatic force between two charged particles in a channel. We then model electroosmotic flow in nanochannels with regular or random roughness on the walls. The mechanism of electrokinetic transport in rough channels is investigated and discussed. Electroosmotic flow is shown to be much more sensitive to wall roughness than pressure driven flow and to be controlled by a new length scale related to the width of the charge distribution. A brief summary and concluding remarks are presented in Section 4.

2. Numerical algorithm

2.1. Nonequilibrium molecular dynamics

We use nonequilibrium molecular dynamics (NEMD) to simulate electroosmotic flows. The simulation domain contains particles representing fluid molecules, ions and atoms (charged and neutral), between bounding solid walls. Flat walls are formed from three layers of solid atoms arranged to form a (111) surface of a FCC crystal structure. Rough walls are made by continuing the structure to different heights. All the solid atoms are held stationary throughout the simulation.

Short-range van der Waals interactions between all particles are modeled with a truncated and shifted Lennard–Jones (LJ) potential,

$$V^{\mathrm{LJ}}(r) = 4\epsilon\left[\left(\frac{\sigma}{r}\right)^{12} - \left(\frac{\sigma}{r}\right)^{6} - \left(\frac{\sigma}{r_{c,\mathrm{LJ}}}\right)^{12} + \left(\frac{\sigma}{r_{c,\mathrm{LJ}}}\right)^{6}\right], \tag{1}$$

where r is the separation between particles, ϵ the characteristic binding energy and σ the atomic diameter. Setting the interaction to zero beyond the cutoff distance $r_{c,\mathrm{LJ}} = 2.5\sigma$ has little effect on the dynamics and reduces the computational cost [27]. We use the same σ for interactions between all particles, but allow for a different interaction strength ϵ_{wf} between wall and fluid atoms. Ions and fluid atoms interact with the same ϵ.

We assign a charge of $\pm e$ (e is the electron charge 1.6×10^{-19} C) to every ion in the fluid. The innermost solid atoms, which are closest to the fluid, are uniformly charged to ensure an electrically neutral system. The long-range Coulomb potential between charged particles is

$$V^{C}(r) = \frac{q_i q_j}{4\pi\epsilon_0\epsilon_r r}, \tag{2}$$

where q_i and q_j are the charges for particles i and j, respectively. The vacuum permittivity is ϵ_0 and there is a uniform dielectric constant ϵ_r throughout the simulation cell. A dielectric contrast between solvent and solid could be included, but would require information about the spatial variation of ϵ_r or use of polarizable potentials. Unlike the Lennard–Jones potential, the Coulomb potential is not cut off because this is known to affect simulations [27]. The long-range Coulomb force makes the numerical simulation of large systems extremely expensive.

We integrate the equations of motion for particles using the Verlet scheme [27]. The time step is $\Delta t = 0.005\tau$, where $\tau = (m\sigma^2/\epsilon)^{1/2}$ is the characteristic time of the Lennard–Jones potential. A Langevin thermostat [28] with damping rate $1.0\tau^{-1}$ is applied in the flow irrelevant y direction to ensure a constant temperature of $T = 1.1\epsilon/k_B$, where k_B is Boltzmann's constant. This temperature has been considered in many previous LJ studies and the properties of uncharged systems are well known.

Most results are presented in dimensionless form, using ϵ, σ and τ. The relative importance of Coulomb interactions depends on the dielectric constant, ϵ_r. This can be parameterized in terms of the Bjerrum length $l_B \equiv e^2/(4\pi\epsilon_0\epsilon_r k_B T)$, which is the

separation where electrostatic interactions equal the thermal energy. For water at room temperature $\epsilon_r \approx 80$ and $l_B \sim 0.7$ nm, i.e. a couple of molecular diameters. To accentuate the role of Coulomb interactions in tests of our method, we usually consider $l_B = 7.86\sigma$, corresponding to a dielectric constant that is roughly four times smaller than water and typical of alcohols. Some results for a case closer to water, $l_B = 2.55\sigma$, are also shown for comparison.

2.2. Particle–Particle Particle–Mesh (P^3M) method

As mentioned in the last section, an efficient treatment of the long-range Coulomb force between charges is essential and has been a focus of active research for many years. We adopt the P^3M method proposed by Beckers et al. [24]. In this method the short-range interactions from both Coulomb and van der Waals forces are treated precisely with the Particle–Particle (PP) method while the long-range interactions are calculated with the Particle–Mesh (PM) method. Both the advantages of the accuracy of the PP method and the efficiency of the PM method can be achieved through this approach. Fig. 1 illustrates the typical one time-step loop of the P^3M algorithm.

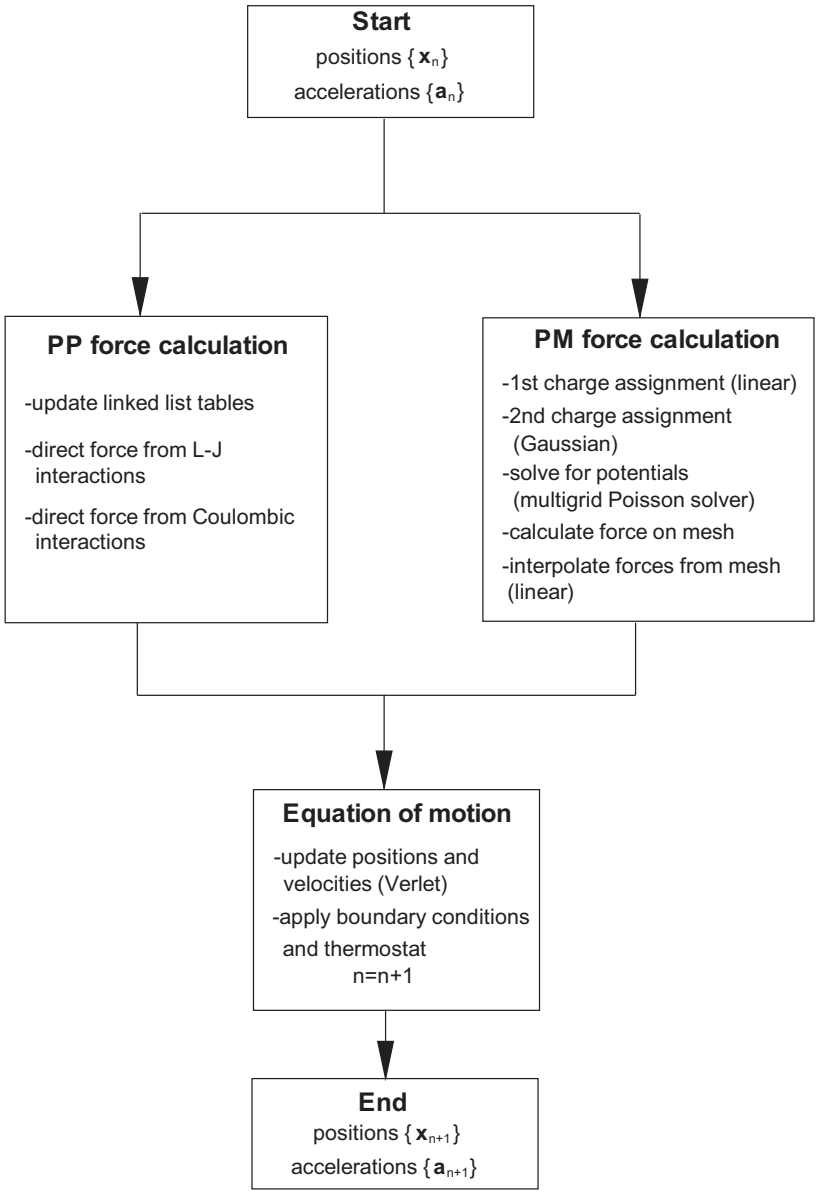

Fig. 1. One time-step loop of the P^3M algorithm.

In P^3M, the total force acting on particle i is split into two parts as:

$$\mathbf{F}_i = \mathbf{F}_i^{PP} + \mathbf{F}_i^{PM}, \tag{3}$$

where $\mathbf{F}_i^{PP}$ represents the short-range force from nearby particles which can be computed through direct summation and $\mathbf{F}_i^{PM}$ represents the long-range force which can be calculated by solving Poisson's equation for the electric potential on a mesh. A two-dimensional schematic of the P^3M is displayed in Fig. 2, but a three-dimensional implementation is used in our simulations.

The short-range force $\mathbf{F}_i^{PP}$ consists of two parts,

$$\mathbf{F}_i^{PP} = \mathbf{F}_i^{LJ} + \mathbf{F}_i^{C}. \tag{4}$$

Here $\mathbf{F}_i^{LJ}$ is the total van der Waals force on particle i from all other particles

$$\mathbf{F}_i^{LJ} = \sum_{j\neq i}^{\Omega_{i,LJ}} \frac{24\epsilon \mathbf{r}_{ij}}{|\mathbf{r}_{ij}|}\left[2\left(\frac{\sigma}{|\mathbf{r}_{ij}|}\right)^{13} - \left(\frac{\sigma}{|\mathbf{r}_{ij}|}\right)^{7}\right], \tag{5}$$

where $\Omega_{i,LJ}$ is the spatial region within the LJ cutoff $r_{c,LJ}$ from particle i. $\mathbf{F}_i^C$ is the total Coulomb force from particles within Coulomb cutoff $r_{c,C}$. $\mathbf{F}_i^C$ contains two parts: the direct Coulomb force from other charged particles and a correction force due to double counting in the short and long-range calculations. The exact form of the correction force depends on the scheme of charge assignment and will be discussed below.

To compute the particle-mesh force $\mathbf{F}_i^{PM}$, we need to solve for the electrostatic potential ϕ on a mesh:

$$\nabla^2\phi(\mathbf{R}) = -\frac{1}{\epsilon_r\epsilon_0}\rho_e(\mathbf{R}), \tag{6}$$

where $\rho_e(\mathbf{R})$ is the charge density at grid point $\mathbf{R}$, and the charge density is defined as the grid point charge per grid cell

$$\rho_e(\mathbf{R}) = \frac{q(\mathbf{R})}{h_x h_y h_z}, \tag{7}$$

where h_x, h_y and h_z are the grid sizes in x, y and z directions, respectively.

We smooth the ion charges onto the mesh points in two steps. In the first step the charge of each ion is assigned to the eight nearest mesh points using a linear weighting function [25]. In the second step, the grid point charges from the first step are further spread out onto the surrounding grid points using a Gaussian assignment function. The width of the Gaussian distribution is set at $\sigma_G = r_{c,C}/3$, where $r_{c,C}$ corresponds to the cutoff distance for Coulomb interactions contributing to F_i^{PP}.

The computation time for the first assignment step is negligible. The second Gaussian assignment step becomes the most time consuming part of the calculation as we refine the mesh size or increase the P ↔ P Coulomb interaction cutoff $r_{c,C}$ [24]. In Ref. [24], the authors proposed a strategy of solving a diffusion equation to alleviate the problem. In this work, we

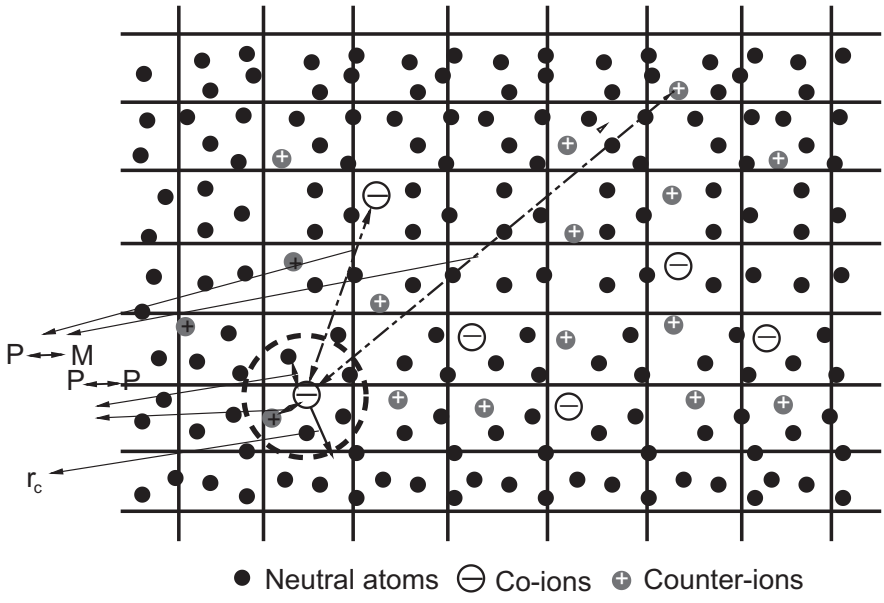

Fig. 2. A two-dimensional schematic of the P^3M algorithm. The simulations are actually three-dimensional. Lines indicate the mesh which has spacing h_x and h_y along horizontal and vertical directions. Short-range contributions (P ↔ P) are obtained by direct summation over nearby particles with a radius r_c (dashed circle). Long range contributions (P ↔ M) are obtained from the particle–mesh method.

overcome this problem by adopting the method proposed by Shan et al. [29]. This method is based on the separability property of the Gaussian, it allows us to spread the charge distribution in three one-dimensional operations instead of one three-dimensional operation. This reduces the number of operation steps to $3 \times N_g$ instead of N_g^3, where N_g is the number of grids within the cutoff range in one direction. Implementation of this method dramatically reduces the computational time associated with second charge assignment and therefore allows us to use a finer mesh or larger cutoff distance to improve the accuracy.

The Poisson equation for the electrostatic potential (Eq. (6)) is solved using an iterative multi-grid approach. Thus the initial values of the potential play a key role in improving the efficiency of the solver. Better initial values mean fewer iteration steps. In our code, as in [24], we store the potential at two previous time steps and use an Euler forward scheme to obtain a good initial guess:

$$\phi(t) = \phi(t - \Delta t) + (\phi(t - \Delta t) - \phi(t - 2\Delta t)). \tag{8}$$

After solving for the electric potential ϕ, the electric field on the grid points can be calculated by taking the derivative of ϕ using the second-order centered-difference,

$$\mathbf{E}(\mathbf{R}) = -\nabla\phi(\mathbf{R}). \tag{9}$$

Then the electric field $\mathbf{E}(\mathbf{r}_i)$ at $\mathbf{r}_i$ can be obtained by linear interpolation from the eight nearest mesh points using exactly the same approach as in the first step of the charge assignment. The long-range particle force on particle i is then:

$$\mathbf{F}_i^{\mathrm{PM}} = q_i \mathbf{E}(\mathbf{r}_i). \tag{10}$$

Finally the total Coulomb force from particles near particle i in Eq. (4) can be computed as:

$$\mathbf{F}_i^C = \sum_{j \neq i}^{\Omega_{i,C}} \frac{q_i q_j \mathbf{r}_{ij}}{4\pi\epsilon_r\epsilon_0 |\mathbf{r}_{ij}|^3} \left[1 + \frac{2|\mathbf{r}_{ij}|}{\sqrt{\pi}\sigma_G} \exp\left(-\frac{|\mathbf{r}_{ij}|^2}{\sigma_G^2} \right) - \mathrm{erf}\left(\frac{|\mathbf{r}_{ij}|}{\sigma_G} \right) \right]. \tag{11}$$

where $\Omega_{i,C}$ defines the interaction domain according to the Coulomb cutoff $r_{c,C}$ and erf (x) is the error function. The last two terms in Eq. (11) represent the correction force and are derived from the second charge Gaussian assignment.

2.3. Multi-grid solver for Poisson equation

Since we have to solve the Poisson equation for the electric potential at every time step, an efficient and robust Poisson solver is crucial for the total performance of the P^{3}M scheme. Beckers et al. [24] adopted the conventional SOR method to solve the Poisson equation in their P^{3}M scheme, while more recently Aboud et al. [30] implemented a multi-grid Poisson solver in their P^{3}M scheme to simulate ionic liquids. Using their scheme, they have successfully calculated the thermodynamic properties of electrolyte solutions and examined the charge distribution profile for systems containing a lipid membrane. In our algorithm, we also use a multi-grid Poisson solver due to its superior convergence properties relative to the SOR method.

The multi-grid method is a well-established approach for solving differential equations in an iterative way. Implementation of the multi-grid method with different discretizations of the domains can be found in Refs. [31–34]. In principle, the discretized Poisson equation is solved on a hierarchy of mesh points with varying sizes. The central procedure in the multi-grid method is the so-called V-cycle. It contains three major operations: smoothing on each level of grids, restriction from fine to coarse grids and prolongation from coarse to fine grids. Since the equations are solved on different levels of grids at each step, the errors associated with different Fourier modes at different scales can be reduced simultaneously. As a result, the multi-grid method has a much better convergence rate than the SOR method. Another attractive merit of the multi-grid method is that because the method solves the equations on multiple scales, it can naturally be incorporated into multiscale simulation methods. Building on our previous multiscale schemes for simple fluids [42,45] and the multi-grid approach presented here, we are currently developing a novel methodology for systems involving long-range electrostatic interactions based on the idea of "domain decomposition" and "constrained dynamics".

2.4. Boundary conditions

Our goal is to solve the equations for slablike geometries with periodic boundary conditions in the plane of the solid walls. Methods for treating boundary conditions in the non-periodic direction have been a research topic for many years. A two-dimensional Ewald summation method (EW2D) was first introduced by Parry [35] and was considered to be the most accurate. However, a direct application of the EW2D method has proved to be very computationally expensive [36–38]. An alternative approach is to extend the non-periodic direction to create a sufficiently large empty space and then impose periodic boundary conditions in all three directions. The conventional techniques for solving electrostatic fields such as the three-dimensional Ewald summation method (EW3D) and the P^{3}M method can then be employed. The purpose of including empty space in the non-periodic direction is to avoid artificial effects caused by interactions between periodic images in that direction. However, as pointed out in Ref. [38], even though results from EW3D with periodic boundary conditions in all three directions slowly converge to results from EW2D as the empty space in the non-periodic direction increases, the convergence is unsatisfactory even when the total length in the non-periodic direction is five times larger than the length in the

periodic directions. This means that it is impractical to extend the length in the non-periodic direction and use periodic boundary conditions to obtain satisfactory results.

Yeh and Berkowitz [39] proposed a simple and efficient method for treating systems with slab geometries. In their method, the non-periodic dimension (e.g. the z direction in our case) was first extended to create some empty space, then the periodic boundary conditions were applied in all three directions to calculate interparticle forces. Finally, a correction force was added to each particle to remove the artifacts from the image charges due to periodic boundary conditions. Based on their derivation, the correction force can be calculated as:

$$F_{x,i} = F_{y,i} = 0, \tag{12}$$

$$F_{z,i} = -\frac{q_i}{V} M_z, \tag{13}$$

where V is the volume of the computational domain and M_z is the z component of the dipole moment of the whole system. They demonstrated their method through calculation of forces between two particles and they could reproduce the EW2D results using the EW3D method plus the correction. They also suggested an empty space of at least L_x or L_y for their method to work. In our algorithm we adopt their method due to its simplicity and efficiency.

3. Results and discussions

3.1. Verification of the algorithm

To verify our P^{3}M scheme for long-range Coulomb interactions and the treatment of the boundary conditions for slablike geometries, we calculate the Coulomb force between two particles with opposite charges. This is considered to be the most straightforward and accurate test of different treatments for the long-range force and has also been used in Refs. [38,39].

Periodic boundary conditions are imposed in the x and y directions with periods $L_x = 10.43\sigma$ and $L_y = 12.04\sigma$, respectively. The dimension in the z direction is $L_z = 4L_x = 41.72\sigma$. As discussed in Section 2.4, we first calculate forces assuming periodic boundary conditions along z and then subtract the effect of periodic images using the correction in Eq. (13). The accuracy of the P^{3}M approach can always be improved by refining the mesh size or increasing the cutoff distance $r_{c,C}$, but this increases the computational cost. In this test of the algorithm we use the same parameters as in later simulations. The mesh size is about 1σ and the cutoff is $r_{c,C} = 8\sigma$.

We present results for two charges separated by z and placed at $(L_x/2, L_y/2, L_z/2 + z/2)$ and $(L_x/2, L_y/2, L_z/2 - z/2)$, but similar results were obtained for other separation directions. Fig. 3 shows the force as a function of separation before (triangles) and after (squares) correcting for periodic boundary conditions. At small separations, both results approach the bare Coulomb force $F_z = e^2/(4\pi\epsilon_r\epsilon_0 r^2)$ (solid line). When the separation becomes large compared to L_x and L_y, the interaction between the periodic images of the charges becomes equivalent to the interaction between two charged surfaces. The force approaches a constant that can be calculated analytically: $F_z = e^2/(2\epsilon_r\epsilon_0 L_x L_y)$. After correcting with Eq. (13), the numerical results are in

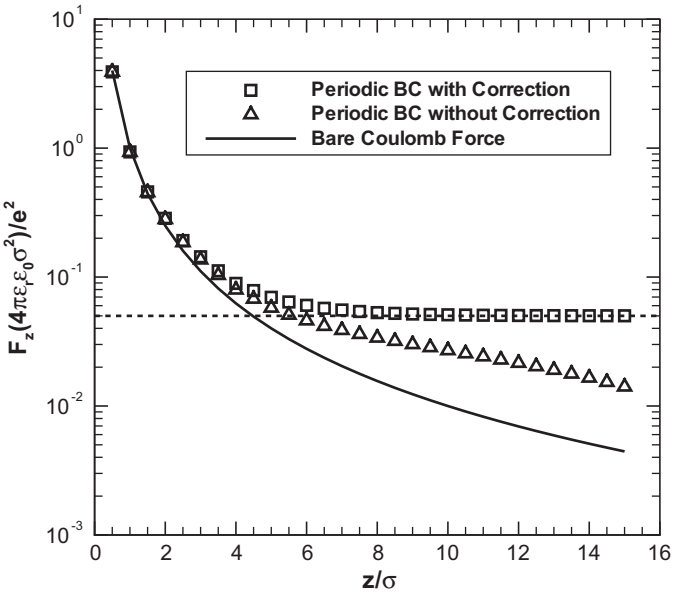

Fig. 3. Force between two charges as a function of distance. Numerical results before (triangles) and after (squares) correcting for periodic images along z are compared to the bare Coulomb interaction (solid line) and analytic limit $e^2/2\epsilon_0\epsilon_r L_x L_y$(dashed line) for large separations.

excellent agreement with this asymptotic result (dashed line). Merely increasing the empty space without applying the correction does not lead to accurate results. When the correction is included, an empty space on the order of the larger of L_x and L_y is sufficient for good numerical results as concluded in Ref. [39].

3.2. Electroosmotic flows in nanoscale rough channels

Roughness on solid walls is ubiquitous in nature. It is now well accepted that this roughness can dramatically affect nanoscale flows [40]. The many applications of electroosmotic flows have inspired recent studies of the effect of roughness on electroosmotic flows using continuum methods [6,7,11]. These methods may fail at the nanoscale due to the inherent assumptions in continuum equations. To overcome these limitations, Kim and Darve [14] and Qiao [17] have performed molecular simulations of electroosmotic flows in rough channels. They constructed the roughness as regular squares on top of the walls and found that the charge distribution and flow rate could be significantly affected by the roughness. However a systematic study of the effect of surface charge density and the structure of the roughness was not presented in these papers. In this section, we will implement our P^{3}M approach to simulate electroosmotic flows in rough channels and attempt to address these and related issues.

3.2.1. Rectangular bumps

Fig. 4 illustrates the geometry for our first studies of flow in a rough channel. The fluid is confined between two walls with a separation distance of H. Nanoscale rectangular bumps are added to both the bottom and top walls. These bumps extend across the system in the y direction, have width w along x, and height h. They are constructed by extending the lattice structure of smooth walls. As a result, the height takes on discrete values of $h = n \cdot dz$, where $dz = 0.98\sigma$ is the distance between two successive layers and $n = 1, 2 \ldots$ is the number of added layers.

The region between the two vertical dotted lines in Fig. 4 is the simulation domain. Periodic boundary conditions with period of $L_x = 28.2\sigma$ and $L_y = 9.6\sigma$ are imposed along x and y directions, respectively. The channel height is fixed at $H = 32.4\sigma$. The mesh domain in calculations of the electrostatic force is L_x by L_y by $L_z = 2H$ in x, y and z directions. The flow is driven by an external electrical field E which is parallel to the x direction. We set both the fluid and solid density at $0.81m\sigma^{-3}$. A wall fluid interaction of $\epsilon_{wf} = 0.6\epsilon$ is chosen so that the system satisfies the no-slip boundary condition that is commonly assumed in continuum models.

At the start of the simulations, we randomly choose 50 fluid particles and assign them a positive charge $+e$. We then charge the solid walls to maintain an electrically neutral system. The required surface charge density $\sigma_s = -0.092e/\sigma^2$ is in the experimental range. For flat walls, all of the innermost atoms have equal charges. The same charge is used for rough walls, and charge is not applied to the sides of the bumps. Separate simulations showed that charging the sides had negligible effect on the flow for our simulation parameters.

To quantify the effects of wall roughness on electroosmotic flow, a series of simulations with varying h and w were carried out. The flow rate is computed for each case and compared with the smooth wall result. The volume flow rate per unit width along the y direction is defined as the integral of the velocity over the height of the channel:

$$Q = \int_0^H u(z)dz, \tag{14}$$

where u is the x component of the velocity. In the limit of low driving field E, one expects linear response, $Q \propto E$. We normalize results for rough walls by the smooth wall flux Q_{smooth} and find the ratio is independent of E in the small field limit. As shown below, the flux required to reach this limit is surprisingly small for electroosmotic flows.

For reference purposes, we also performed pressure driven (Poiseuille) flow simulations for exactly the same geometries. A pressure gradient is realized by adding a constant force $-v\frac{dP}{dx}$ along the x direction to each particle, where v is the volume

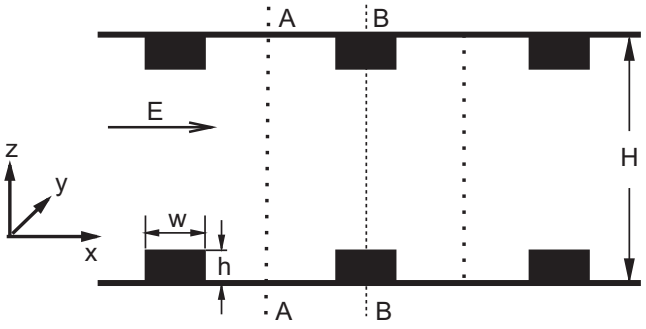

Fig. 4. Schematic of the channel flow geometry. The rectangular bumps on the walls and their dimensions are indicated. One period corresponds to the space between dotted lines and the velocity field along the line A–A is shown in Fig. 6.

per particle. The resulting velocity field is consistent with the analytic solution of the Navier–Stokes equations for Poiseuille flow with flat walls and no-slip boundary conditions:

$$u(z) = \frac{1}{2\mu}\left(-\frac{dP}{dx}\right)(Hz - z^2), \tag{15}$$

where u is along the x axis, μ is the dynamic viscosity and $H = 32.4\sigma$ is the width of the channel. The viscosity $\mu = 2.14\epsilon\tau\sigma^{-3}$ has been calculated in our previous work [41,42]. We apply a pressure gradient $\frac{dP}{dx} = -0.015\epsilon\sigma^{-4}$ so that the fluid velocity at the center of the channel is about $0.9\sigma/\tau$.

Fig. 5 shows the variation of flow rate with the height of the roughness h for electroosmotic and pressure driven flow. In all cases the width of the roughness is fixed at $w = 5.21\sigma$. Both the electroosmotic and pressure driven flows decrease with increasing roughness height. For pressure driven flow, Q decreases roughly linearly with h. Electroosmotic flow drops more dramatically with increasing h. A bump just two layers high reduces the flow by more than 50%. Additional roughness leads to a more gradual drop in flow. As discussed below, the range of h where electroosmotic flow drops rapidly corresponds to the width δ of the charge density, while the only length scales in pressure driven flow are the channel dimensions.

The results for electroosmotic flow have converged to the limiting Newtonian behavior for the smallest flux, $Q = 2.26\sigma^2/\tau$. Increasing the driving field leads to a nonlinear increase in Q_{smooth} and also increases the effect of the roughness. The medium and large fields are factors of 2.5 and 4 times larger than the low field case, while Q_{smooth} increases by factors of 2.76 and 7.69, respectively. In contrast, the pressure driven flow was linear in dP/dx up to much larger fluxes. Results are not shown, but this is consistent with previous studies [43].

The greater sensitivity of electroosmotic flow to roughness and flow rate is connected to the distribution of the driving force and thus derivatives of the flow field. Sample flow fields for pressure and electroosmotic flows are illustrated in Fig. 6. The pressure gradient provides a uniform force and thus a constant curvature in the flow profile (Eq. (15)). The electroosmotic driving force is proportional to the charge density. As shown in Fig. 7, this is sharply peaked near the surface. The resulting flow profile shows a rapid increase in the vicinity of the charge peak, and plug-like flow in the center of the channel. For both types of flow, the velocity gradient is highest near the wall, and non-Newtonian behavior is observed when this gradient, ∇u_{max}, exceeds a common threshold value. However the threshold is always reached at lower fluxes for electroosmotic flow. For this case, the maximum derivative $\nabla u_{max} \approx \delta^{-1}(Q/H)$, where $\delta \sim \sigma$ is the distance over which the velocity rises and Q/H is the mean velocity in the channel. For pressure driven flow $\nabla u_{max} = 6H^{-1}(Q/H)$. Thus the mean velocity for non-Newtonian effects is independent of H for electroosmotic flow, and increases linearly with H for pressure driven flow. This very different scale dependence of the onset of non-Newtonian flow may be an important consideration in device design.

For the parameters used here and in earlier work [43] the threshold value of ∇u_{max} is about $0.1\tau^{-1}$. The threshold may be much lower near the wall for other interactions [44]. We found that high velocity gradients also led to changes in the width

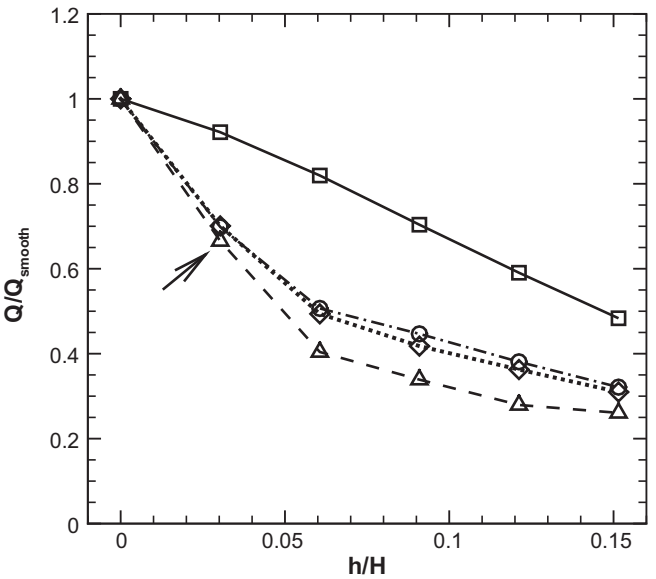

Fig. 5. Sensitivity to roughness height for pressure driven flow (squares) and electroosmotic flow at small (circles), medium (diamonds) and large (triangles) driving fields. Flows are normalized by the flux between smooth walls and the surface charge density for electroosmotic flow is $-0.092e/\sigma^2$. Statistical errors are smaller than the symbol size. The roughness height is normalized by $H = 32.4\sigma$. This collapses results for pressure driven flow at different H (not shown), but electoosmotic results for a given h depend on the width of the charged layer δ and are not sensitive to H. An arrow indicates the case of a single layer bump that is considered in Fig. 6.

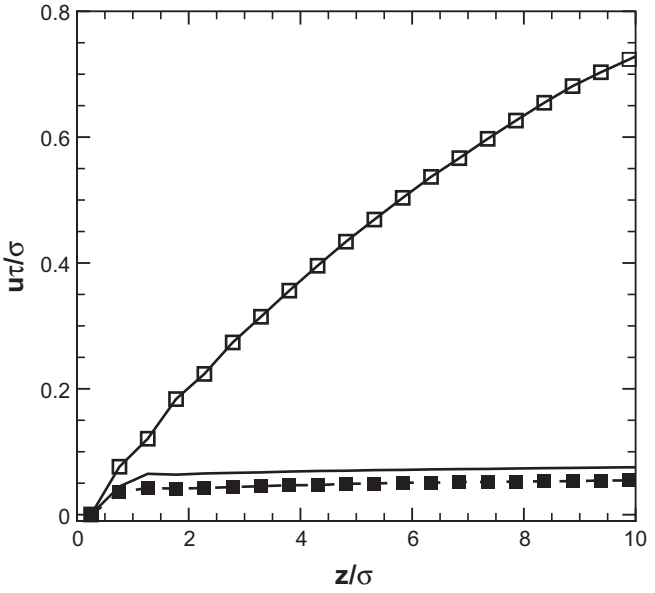

Fig. 6. The streamwise velocity profile for pressure driven flow between smooth walls (open squares connected by solid line) and electroosmotic flow between smooth walls (solid line) and at A–A (Fig. 4) for rough walls (filled squares). Results are for a bump one atomic layer high (arrow in Fig. 5) and are only shown for the region near one wall.

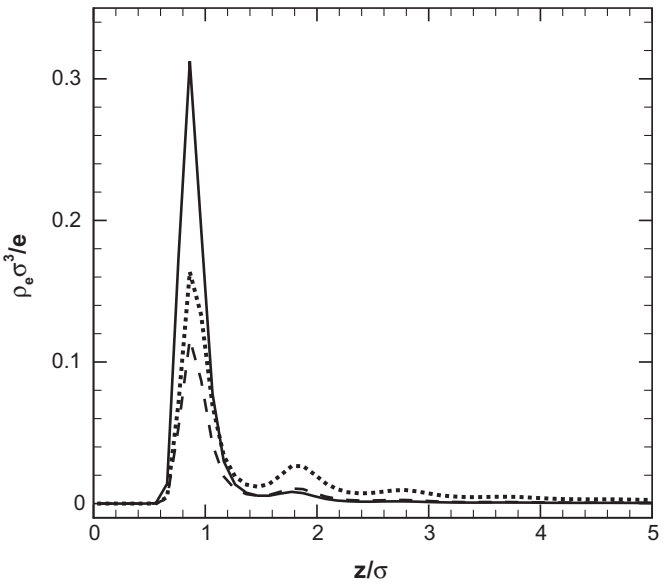

Fig. 7. Charge density profiles for smooth wall cases at different surface charge densities, $-0.046e/\sigma^2$ (dash line) and $-0.092e/\sigma^2$ (solid line), for $l_B = 7.86\sigma$. Results for $-0.092e/\sigma^2$ and a higher ϵ_r corresponding to $l_B = 2.55\sigma$ (dotted line), are also shown. The oscillations at small z are associated with layering in the fluid, with the first layer extending to $z \approx 1.5\sigma$. The charge density near flat sections of rough walls is nearly identical.

of the charge distribution near flat walls. This represents an additional origin for non-Newtonian behavior in electroosmotic flows that does not have a direct parallel in pressure driven flows. This effect began at about the same velocity gradient as other non-Newtonian effects for the parameters used here, but may occur at smaller gradients in other systems.

The greater sensitivity of electroosmosis to roughness is also related to the concentration of the driving force near the wall. Changes in channel width produce small perturbations on the flow profile for pressure driven flow. For electroosmotic flow, the region of high velocity gradient follows the region of high charge and shifts by a height comparable to its width even for a bump that is one atomic layer high. This rapid change in velocity field leads to a large stress. One consequence

is that the central velocity on a line (A-A in Fig. 4) between bumps on a rough wall in Fig. 5 is 25% smaller than that for smooth walls even though the driving force and charge density are indistinguishable. This is discussed further below.

The bump width w also has very different effects on electroosmotic and pressure driven flow. Fig. 8 shows the flux for varying w at a fixed height of $h = 2.95\sigma$ (three layers) and with Q in the Newtonian limit. One might expect the flow rate to decrease with increasing w because the mean width of the channel is decreased. Results for pressure driven flow are consistent with this expectation, but electroosmotic flow is nearly independent of w. This can be understood from the flow profiles in Fig. 6. The flux increases as the cube of the wall spacing for pressure driven flow. If the bump covered the entire wall, the flux would be reduced by a factor of $[(H-2h)/H]^3 = 0.55$. The results for pressure driven flow in Fig. 8 drop towards this limiting value as w increases.

The flux increases only linearly with wall spacing for electroosmotic flow, so a uniform reduction in channel width by $2h$ would only reduce the flux by $(H-2h)/H = 0.82$. The actual flux is less than half this estimate, and nearly independent of w. This implies that most of the decrease in flux is caused from dissipation at the edge of the bump. Direct evaluation of the drag force from the fluid on the wall confirms that this is the case. The drag on the atoms nearest the corner is orders of magnitude larger than that on flat regions.

The scaling of flux with H is also very different for pressure driven and electroosmotic flow. For pressure driven flow, the only length scales are set by the channel dimensions (assuming no-slip boundary conditions). We performed simulations to check that if H and L_x are scaled by the same factor the effect of roughness depends only on h/H and the results collapse on those plotted in Fig. 5. For electroosmotic flow there is an additional length scale δ corresponding to the width of the charge distribution and the range of large velocity gradient. We found that Q/Q_{smooth} was nearly independent of H for a given bump height, indicating that h/δ is the key dimensionless parameter.

As a further test, we have varied δ by changing the charge density σ_s and by increasing the dielectric constant to reduce the relative strength of Coulomb interactions. Fig. 7 shows that the charge density exhibits oscillations that correlate with the layering induced in the total fluid density by the solid walls. Increasing σ_s increases the total charge density, but also decreases δ. For $|\sigma_s| \geqslant 0.138e/\sigma^2$ (not shown), more than 90% of charge is in the first layer ($z < 1.5\sigma$). In contrast, increasing ϵ_r by a factor of 3 ($l_B = 2.55\sigma$) lowers the confining effect of Coulomb forces and increases δ. For this case there is significant density out to 4 or 5 layers.

These trends in charge distribution can be understood in terms of continuum Poisson–Boltzmann (PB) theory. The characteristic length for the charge density to decay is the Gouy–Chapman length $z_0 \equiv 1/(2\pi l_B|\sigma_s|)$. This length shows the trends in Fig. 7, rising as either l_B or $|\sigma_s|$ decrease. However, z_0 remains lower than a lattice constant for the parameters considered in this paper, and PB theory does not include layering, so it is difficult to make a quantitative comparison between z_0 and δ.

Fig. 9 shows that changes in δ have the expected effect on the dependence of flow rate on roughness height. For the highest charge densities, nearly all the charge is in the first layer and most of the reduction in Q occurs for bumps only two layers high. Results for the lowest charge density and for $l_B = 2.55\sigma$ decrease roughly linearly, although with a steeper slope than for

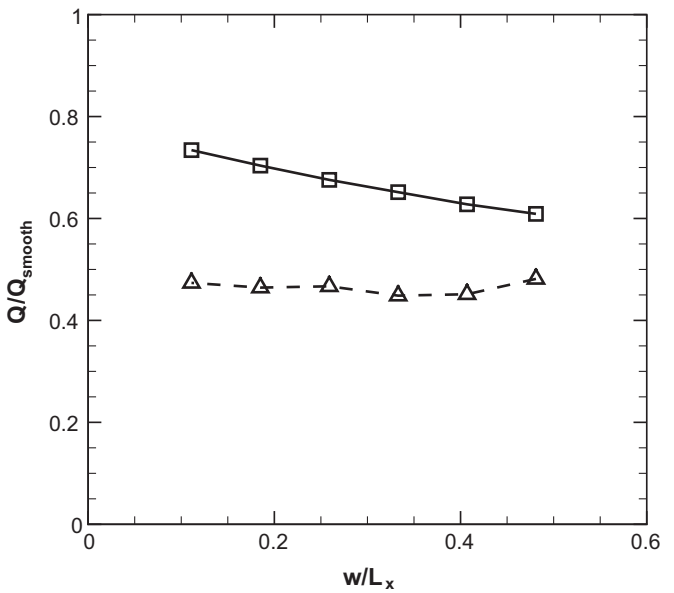

Fig. 8. Variation of flow rate with bump width w at $h = 2.95\sigma$ and the same parameters as Fig. 5. Squares are for pressure driven flow and triangles are for electroosmotic flow at $\sigma_s = -0.092e/\sigma^2$. Statistical errors are smaller than the symbol size.

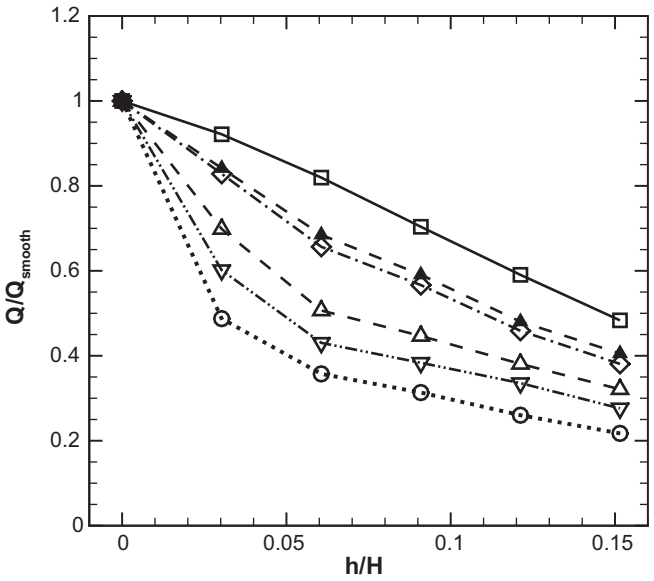

Fig. 9. Variation of flow rate with roughness height h for cases with different δ obtained by varying σ_s and l_B. Results are for $l_B = 7.86\sigma$ and $\sigma_s = -0.046e/\sigma^2$ (open diamonds), $\sigma_s = -0.092e/\sigma^2$ (open triangles), $\sigma_s = -0.138e/\sigma^2$ (open inverted triangles), and $\sigma_s = -0.184e/\sigma^2$ (open circles), and for $l_B = 2.55\sigma$ at $\sigma_s = -0.092e/\sigma^2$ (filled triangles). The pressure driven flow results from exactly the same geometries are also shown for reference (open squares). Statistical errors are smaller than the symbol size.

pressure driven flow. Once more, studies for different H show that results for Q/Q_{smooth} for electroosmotic flow are independent of H while pressure driven flow depends only on h/H. This brings out the importance of varying δ, h and H independently. For sufficiently small H and large δ, the different scaling of pressure driven and electroosmotic flow would not be evident.

The above arguments would suggest that pressure driven flow is more sensitive to reductions in channel width, while electroosmotic flow is more sensitive to sudden changes in wall height. We have tested this with simulations where the mean channel width is the same, but there are two equally spaced bumps of the same height instead of a single bump with twice the length. For the case of $\sigma_s = -0.092e/\sigma^2$ and $l_b = 7.86\sigma$, breaking the bump into two pieces reduces the pressure driven flux by only 7%, while the electroosmotic flux drops by 40%. This pronounced contrast implies that surface smoothness may be critical in electroosmotic devices.

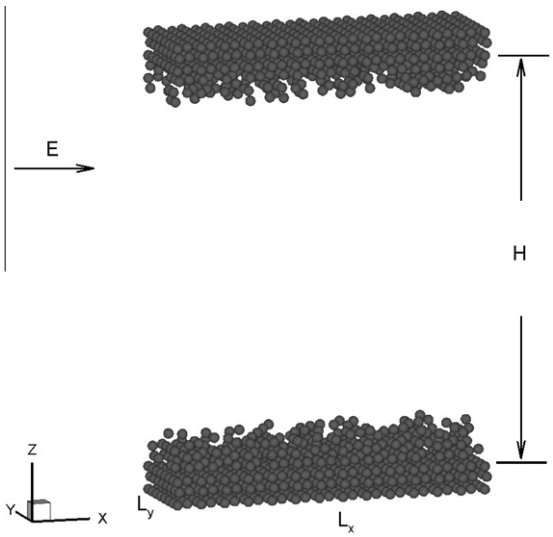

Fig. 10. Geometry of channel with randomly rough walls. The number of additional layers at each point is uniformly distributed so the height changes from 0 to h. In this case $h = 2.95\sigma$.

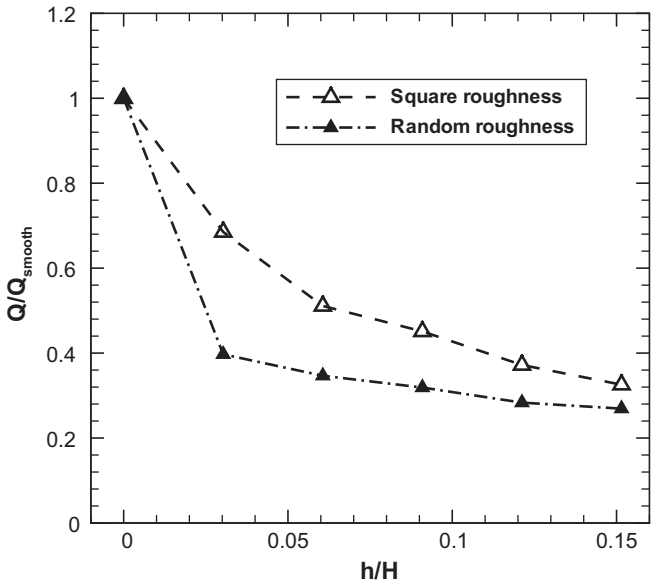

Fig. 11. The variation of flow rate with roughness height h for regular bumps (open symbols) and random roughness (filled symbols). The regular bump covers half the surface $w = L_x/2$ so the mean height of both surfaces is $h/2$. The surface charge density is $-0.092e/\sigma^2$ and statistical errors are smaller than the symbol size.

3.2.2. Random roughness

The above simulations considered regular rectangular bumps rather than the irregular and random roughness that is more likely to be found on experimental surfaces. In this section we consider a simple model for a random rough wall. The height at each coordinate (x,y) in the plane of the wall varies from 0 to n_h layers, with the heights determined from a uniformly distributed random number generator. This method is easy to implement, and can be improved to be closer to reality by incorporating height correlations. Fig. 10 shows a typical channel with random roughness on both top and bottom walls.

Fig. 11 shows a comparison between random roughness and rectangular bumps at a surface charge density of $\sigma_s = -0.092e/\sigma^2$. The regular bump has $w = L_x/2$ so that the mean height of both surfaces is $h/2$. The randomly rough walls clearly reduce the flow more than regular bumps. This may be expected from the earlier observation that two bumps with half the width slowed flow much more than a single wide bump. The flow rate is actually similar to the two bump case with the same mean height even though the height changes much more frequently. This suggests that local height changes that allow flow around obstacles in the y direction are less effective in blocking flow than obstacles that extend along y.

As pointed out above, the randomly rough wall in our simulations has no correlations in local height. Recently Wang and Kang [46] proposed a novel strategy to generate random rough walls based on the random generation-growth method in porous media. They have systematically discussed the random structure effect on electroosmotic channel flows using continuum flow models. It would be interesting to extend these studies to molecular scales using our method.

4. Conclusions

We have developed an efficient algorithm for molecular simulation of electrokinetic flows. In this algorithm we calculate the long-range Coulomb interactions using the P^3M method and the Poisson equation for electric potential distribution is solved in physical space using an iterative multi-grid technique. Compared with the traditional SOR method, the multi-grid method has a much better convergence rate and its computational cost scales as $O(N_G)$. We have further improved the efficiency of the algorithm by reducing the computational time associated with the second charge assignment step based on the separability of Gaussians. Another advantage of using the multi-grid Poisson solver is that the whole scheme can be naturally embedded into multiscale hybrid schemes based on "domain decomposition". We are currently developing multiscale hybrid methods for problems involving long-range interactions.

The algorithm was used to study electroosmotic flow in nanochannels with regular or random roughness. Results for regular rectangular bumps show several differences between pressure driven and electroosmotic flow that may be important in device operation. One is that non-Newtonian flow sets in at a much lower volume flux for electroosmotic flow. Electroosmosis produces a high velocity gradient confined to a region of width δ near the walls, while pressure driven flow has a parabolic profile. Non-Newtonian behavior sets in at the same value of the velocity gradient in both cases, but the ratio between electroosmotic and pressure driven fluxes (or mean velocities) needed to reach this criterion scales as δ/H. The maximum

flux in the Newtonian regime scales only as H for electroosmotic flow, but as H^2 for pressure driven flow, and this may constrain electroosmotic devices as the channel width increases.

Roughness also produced much more dramatic changes for electroosmotic flow than pressure driven flow. Pressure-driven flow dropped roughly linearly with roughness height, while electroosmotic flow dropped abruptly and was cut in half by bumps only two molecular layers high in many cases. The origin of this difference was determined by varying the width w and height h of the bumps, as well as the channel width H and width of the charge distribution δ. The latter shows the same trends as the Gouy–Chapman length of Poisson–Boltzmann theory, but is too short for quantitative comparison of the charge density with continuum theory.

Since the fluid exhibits no-slip boundary conditions, the only lengths controlling pressure driven flow are the channel dimensions. Increasing h and w constricts flow by reducing the effective channel width. The net flux is roughly equal to the value obtained by averaging over channel widths along the wall, and results for Q/Q_{smooth} for different H collapsed when plotted in terms of h/H.

The ratio of the roughness height h to the width of the charge distribution δ plays the key role in electroosmotic flow. For the first case considered here (Fig. 5), most of the charge was in the first fluid layer. Bumps only one or two molecular layers high diverted the entire region of high velocity gradient, leading to significant drag. The drag nearly doubled when a single bump was replaced by two with half the width, and very large forces were exerted on atoms near the sides of the bumps. Increasing δ by lowering the surface charge or increasing the dielectric constant (lowering l_B), increased the roughness height needed to produce significant drag. In contrast to pressure driven flow, changes in channel width H had little effect on the ratio of fluxes for smooth and rough walls.

Experimental surfaces are more likely to have random roughness than regular bumps. Studies of simple randomly rough surfaces showed that they reduced electroosmotic flow more than bumps. This may be expected from the greater sensitivity of electroosmotic flow to height changes rather than channel constriction. This pronounced contrast implies that surface smoothness may be critical in electroosmotic devices. Studies considering different height correlations of the roughness would provide further information about the factors that control device performance.

Acknowledgement

This material is based upon work supported by the National Science Foundation under Grant No. CMMI 0709187. The authors thank Prof. J.C. Xu and Prof. L. Chen for helpful discussions on the multi-grid method and thank LANL's LDRD Project 20080727PRD2 for support through the J. R. Oppenheimer Fellowship awarded to M.Wang.

References

[1] K.A. Sharp, B. Honig, Electrostatic interactions in macromolecules: theory and applications, Annu. Rev. Biophys. Biophys. Chem. 19 (1990) 310–332.
[2] B. Honig, A. Nicholls, Classical electrostatics in biology and chemistry, Science 268 (1995) 1144–1149.
[3] C. Yang, D.Q. Li, Analysis of electrokinetic effects on liquid flow in rectangular microchannels, Colloids Surf. A 143 (1998) 339–353.
[4] D.Q. Li, Electro-viscous effects on pressure-driven liquid flow in microchannels, Colloids Surf. A 195 (2001) 35–57.
[5] D.Q. Li, Electrokinetics in Microfluidics, Academic, Oxford, 2004.
[6] Y.D. Hu, C. Werner, D.Q. Li, Electrokinetic transport through rough microchannels, Anal. Chem. 75 (2003) 5747–5758.
[7] Y.D. Hu, C. Werner, D.Q. Li, Influence of the three-dimensional heterogeneous roughness on electrokinetic transport in microchannels, J. Colloid Interf. Sci. 280 (2004) 527–536.
[8] J.K. Wang, M. Wang, Z.X. Li, Lattice Boltzmann simulations of mixing enhancement by the electro-osmotic flow in microchannels, Mod. Phys. Lett. B 19 (2005) 1515–1518.
[9] Z.L. Guo, T.S. Zhao, Y. Shi, A lattice Boltzmann algorithm for electro-osmotic flows in microfluidic devices, J. Chem. Phys. 112 (14) (2005) 144907.
[10] J.K. Wang, M. Wang, Z.X. Li, Lattice Poisson–Boltzmann simulations of electro-osmotic flows in microchannels, J. Colloid Interf. Sci. 296 (2) (2006) 729–736.
[11] M. Wang, J.K. Wang, S.Y. Chen, Roughness and cavitations effects on electro-osmotic flows in rough microchannels using lattice Poisson–Boltzmann methods, J. Comput. Phys. 226 (2007) 836–851.
[12] R. Qiao, N.R. Aluru, Ion concentrations and velocity profiles in nanochannel electroosmotic flows, J. Chem. Phys. 118 (10) (2003) 4692–4701.
[13] A.P. Thompson, Nonequilibrium molecular dynamics simulation of electro-osmotic flow in a charged nanopore, J. Chem. Phys. 119 (14) (2003) 7503–7511.
[14] D. Kim, E. Darve, Molecular dynamics simulation of electro-osmotic flows in rough wall nanochannels, Phys. Rev. E 73 (2006) 051203.
[15] M. Wang, J. Liu, S.Y. Chen, Similarity of electroosmotic flows in nanochannels, Mol. Simul. 33 (2007) 239–244.
[16] M. Wang, J. Liu, S.Y. Chen, Electric potential distribution in nanoscale electroosmosis: from molecules to continuum, Mol. Simul. 33 (2007) 1273–1277.
[17] R. Qiao, Effects of molecular level surface roughness on electroosmotic flow, Microfluid. Nanofluid. 3 (2007) 33–38.
[18] A.Y. Toukmaji, J.A. Board Jr., Ewald summation techniques in perspective: a survey, Comput. Phys. Commun. 95 (1996) 73–92.
[19] P. Ewald, Evaluation of optical and electrostatic lattice potentials, Ann. Phys. 64 (1921) 253–287.
[20] J.W. Perram, H.G. Petersen, S.W. de Leeuw, An algorithm for simulation of condensed matter which grows as the 3/2 power of the number of particles, Mol. Phys. 65 (1988) 875–889.
[21] T. Darden, D. York, L. Pedersen, Particle mesh Ewald: an $N\cdot\log(N)$ method for Ewald sums in large systems, J. Chem. Phys. 98 (1993) 10089–10092.
[22] L. Greengard, V. Rokhlin, A fast algorithm for particle simulations, J. Comput. Phys. 73 (1987) 325–348.
[23] E.L. Pollock, J. Glosli, Comments on P^3M, FMM, and the Ewald method for large periodic Coulombic systems, Comput. Phys. Commun. 95 (1996) 93–110.
[24] J.V.L. Beckers, C.P. Lowe, S.W. de Leeuw, An iterative PPPM method for simulating Coulombic systems on distributed memory parallel computers, Mol. Simul. 20 (1998) 369–383.
[25] R.W. Hockney, J.W. Eastwood, Computer Simulation Using Particles, McGraw-Hill, New York, 1981.
[26] B.A. Luty, W.F. van Gunsteren, Calculating electrostatic interactions using the Particle–Particle Particle–Mesh method with nonperiodic long-range interactions, J. Phys. Chem. 100 (1996) 2581–2587.
[27] M.P. Allen, D.J. Tildesley, Computer Simulation of Liquids, Clarendon Press, Oxford, 1987.

[28] G.S. Grest, K. Kremer, Molecular dynamics simulation for polymers in the presence of a heat bath, Phys. Rev. A 33 (1986) 3628–3631.
[29] Y. Shan, J.L. Klepeis, M.P. Eastwood, R.O. Dror, D.E. Shaw, Gaussian split Ewald: a fast Ewald mesh method for molecular simulation, J. Chem. Phys. 122 (2005) 054101. 1–13.
[30] S. Aboud, D. Marreiro, M. Saraniti, R. Eisenberg, A Poisson P^3M force field scheme for particle-based simulations of ionic liquids, J. Comput. Electron. 3 (2004) 117–133.
[31] W. Hackbush, Multi-Grid Methods and Applications, Springer-Verlag, Berlin, 1985.
[32] P. Wesseling, An Introduction to Multigrid Methods, J. Wiley, New York, 1991.
[33] J. Xu, Iterative methods by space decomposition and subspace correction, SIAM Rev. 34 (1992) 581–613.
[34] S. Shu, D. Sun, J. Xu, An algebraic multigrid method for higher-order finite element discretizations, Computing 77 (2006) 347–377.
[35] D.E. Parry, The electrostatic potential in the surface region of an ionic crystal, Surf. Sci. 49 (1975) 433–440.
[36] S.Y. Liem, J.H.R. Clarke, Calculation of Coulomb interactions in two-dimensionally periodic systems, Mol. Phys. 92 (1997) 19–25.
[37] A.H. Widmann, D.B. Adolf, A comparison of Ewald summation techniques for planar surfaces, Comput. Phys. Commun. 107 (1997) 167–186.
[38] E. Spohr, Effect of electrostatic boundary conditions and system size on the interfacial properties of water and aqueous solutions, J. Chem. Phys. 107 (1997) 6342–6348.
[39] I. Yeh, M.L. Berkowitz, Ewald summation for systems with slab geometry, J. Chem. Phys. 111 (1999) 3155–3162.
[40] G.E. Karniadakis, A. Beskok, Micro Flows, Springer-Verlag, Berlin, 2002.
[41] X.B. Nie, S.Y. Chen, W. E, M.O. Robbins, A continuum and molecular dynamics hybrid method for micro- and nano-fluid flow, J. Fluid Mech. 500 (2004) 55–64.
[42] J. Liu, S.Y. Chen, X.B. Nie, M.O. Robbins, A continuum-atomistic simulation of heat transfer in micro- and nano-flows, J. Comput. Phys. 227 (2007) 279–291.
[43] P.A. Thompson, M.O. Robbins, Shear flow near solids: epitaxial order and flow boundary conditions, Phys. Rev. A 41 (1990) 6830–6837.
[44] P.A. Thompson, S.M. Troian, A general boundary condition for liquid flow at solid surfaces, Nature 389 (1997) 360–363.
[45] J. Liu, S.Y. Chen, X.B. Nie, M.O. Robbins, A continuum-atomistic multi-timescale algorithm for micro/nano flows, Commun. Comput. Phys. 4 (2008) 1279–1291.
[46] M. Wang, Q. Kang, Electrokinetic transport in microchannels with random roughness, Anal. Chem. 81 (2009) 2953–2961.